[6]

A vaporization model for iron/silicate fractionation in the Mercury protoplanet

Bruce Fegley, Jr. [1] and A.G.W. Cameron [2]

[1] *Department of Earth, Atmospheric, and Planetary Sciences, Massachusetts Institute of Technology, Cambridge, MA 02139 (U.S.A.)*
[2] *Center for Astrophysics, 60 Garden Street, Cambridge, MA 02138 (U.S.A.)*

A study has been carried out of the vaporization of a totally molten silicate magma of chondritic composition heated into the range 2500–3500 K. The motivation for this was to determine the changes in the composition of the mantle that would occur in the Mercury protoplanet should that body have been subjected to the high-temperature phase in the evolution of the primitive solar nebula, but the results are of more general interest. We have used both ideal and nonideal descriptions of the magma chemistry. An empirical model, based on ideal mixing of complex components, developed by Hastie and co-workers, was used to describe the nonideal magma. Comparison of our results of the nonideal magma calculations with experimental work on vaporization of chondritic material shows generally good agreement. We find that vaporization of about 70–80% of the original amount of silicate from a chondritic planet is required to produce an iron-rich body with a mean uncompressed density equal to that deduced for Mercury (5.3 g/cm^3). At this point the silicate is depleted in the alkalis, FeO, and SiO_2, and enriched in CaO, MgO, Al_2O_3, and TiO_2 relative to chondritic material. We also predict the production of unique trace element abundance patterns which are depleted in easily oxidized elements relative to other trace elements of similar volatilities.

1. Introduction

Urey [1,2] first noted that the anomalously high density of the planet Mercury implies an iron to silicate ratio larger than that for any other terrestrial planet. In fact the mean density of 5.44 g/cm^3 (uncompressed ~ 5.3 g/cm^3) implies an iron to silicate mass ratio of about 66:34 to 70:30, which is about twice as large as that of any of the other terrestrial planets, the Moon, and the Eucrite Parent Body [3]. By comparison, the mean density of the Earth is 5.52 g/cm^3, corresponding to an uncompressed density of ~ 4.45 g/cm^3 [4].

Many models (falling into two broad classes) have been advanced to account for Mercury's anomalous composition. The first class of models relies on differing physical properties (e.g., density, ferromagnetism, mechanical strength) of iron and silicates to achieve the required iron/silicate fractionation [5–9]. The second class of models invokes the differing volatilities of iron and silicates to fractionate the two phases [4,10–12]. Both equilibrium condensation [4] and vaporization [10–12] models are included within the second class.

The relative merits and demerits of these (and related) scenarios have been discussed in the literature and need not be repeated here. However, we wish to emphasize an important distinction between the two broad classes of models. In the first class of models where physical fractionations of iron and silicates (but essentially no chemical fractionations) occur, we would expect that Mercury would be composed of iron plus essentially chondritic silicates, with a diminution of the total mass. In the second class of models, where volatility effects lead to extensive chemical fractionations, we would expect that the silicate phase in Mercury would undergo large compositional changes as a function of the extent of vaporization (or condensation) and that this evolved composition may later be diluted by infalling planetesimals composed of essentially chondritic silicates. These compositional differences are an important means of distinguishing between the proposed models and are potentially testable by a future Mercury mission. It is therefore of interest to examine quantitatively the consequences of vaporization using current models of solar nebula

physics and chemistry and current knowledge of oxide and silicate chemistry at high temperatures.

Cameron [12] has recently proposed that, during the evolution of the solar nebula, temperatures at the position of formation of Mercury were probably in the range of 2500–3500 K. Should a protoplanetary form of Mercury have been formed early in the history of the primitive solar nebula (presumably by precipitation in a giant gaseous protoplanet, forming a refractory molten silicate and iron body at the center, followed by evaporation of the overlying gaseous envelope); then it would be subjected to this temperature range for a time of the order of a few times 10^4 years [13]. The radiative energy input to the planet is more than sufficient to vaporize the entire mantle. The planet is also situated in a strong solar nebula wind, composed of both a fixed and a fluctuating component, with a relative velocity of the order of 1 km/s. Cameron has argued that this wind may be able to carry away most of the vaporized mantle of the planet, although the process satisfies the energy requirements for this only marginally.

The temperature range 2500–3500 K is above the liquidus temperatures (at 1 bar) of chondritic silicates and refractory mineral assemblages in Ca,Al-rich inclusions, leading to the reasonable assumption that the silicate phase of protomercury would be a silicate magma under these conditions. However, these preliminary calculations [12] referred to the vaporization of a silicate magma with the composition $MgSiO_3$ and did not attempt to examine the vaporization chemistry of more complex silicate materials. We have therefore carried out a series of calculations to study the compositional evolution of a silicate magma (with initial composition approximately being chondritic) as a function of the extent of vaporization. The calculations lead to specific predictions about the present-day bulk composition of Mercury, and also allow a comparison with bulk composition predictions of the equilibrium condensation model [3,4]. We first describe the vaporization model which we used and then compare its predictions with the available observational data and with predictions of the equilibrium condensation model. Finally, some possible spacecraft experiments which may be able to distinguish between competing hypotheses for the iron/silicate fractionation of Mercury are also suggested.

2. Silicate magma vaporization model

2.1. Description of thermodynamic model

We calculated the composition of a totally molten silicate magma and of the vapor phase in equilibrium with it using a multicomponent gas-melt chemical equilibrium code (MAGMA) based on the silicate melt solution models developed by Hastie and coworkers [14–17]. The present calculations were done as a function of the degree of vaporization at 2500–3500 K. Both ideal and nonideal magma solution models were studied.

The initial composition of the magma was assumed to be a mixture of the oxides SiO_2-MgO-CaO-Al_2O_3-TiO_2-Na_2O-K_2O-FeO-UO_2-ThO_2-PuO_2 in relative solar proportions [18] except for FeO which was initially set to 0.1 times the MgO abundance. The remainder of the Fe solar abundance was assumed to form the core of protomercury. The actinides and K were included in the calculations to study the effect of vaporization on the amounts of heat-producing radionuclides left in the planet after partial vaporization. Inclusion of the alkalis also provides a comparison with Hastie's work [14–17]. The use of a more refractory starting composition would not significantly affect the results of our calculations. Such compositions are in fact intermediate compositions produced during the vaporization process.

The vaporization of the pure molten oxides can be written as:

$$M_xO_y(\text{liq}) = xM(g) + yO(g),\qquad(1)$$
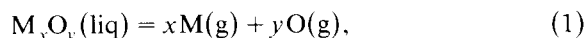
where M is a metal. One such equation is written for each of the 11 metal oxides in the magma. The equations and the corresponding thermodynamic data are listed in Table 1. The vaporization equilibria were calculated by iteratively solving a set of nonlinear simultaneous equations for the abundances of the 11 metals and oxygen in the gas subject to the dual constraints that the ratio of oxygen to metals in the gas must be the same as in the vaporized material from the underlying mantle and that the thermodynamic activities of the 11 metal oxides in the magma must be fitted by the calculations. The equilibrium distribution of the 11 metals and oxygen among different gaseous species was also calculated by the MAGMA code. A total of 37 gases, which are listed in Table 2 with the corresponding thermodynamic data, were

TABLE 1

Thermodynamic data for pure liquid oxide vaporization to constituent atoms ($\log_{10} K = A + B/T$)

Reaction	A	B	Sources
$SiO_2(liq) = Si(g) + 2O(g)$	22.13	−94311	[19,20]
$MgO(liq) = Mg(g) + O(g)$	12.56	−46992	[19,20]
$FeO(liq) = Fe(g) + O(g)$	12.06	−44992	[19,20]
$CaO(liq) = Ca(g) + O(g)$	11.88	−49586	[19,20]
$Al_2O_3(liq) = 2Al(g) + 3O(g)$	35.83	−153255	[20]
$TiO_2(liq) = Ti(g) + 2O(g)$	21.07	−95362	[19,20]
$Na_2O(liq) = 2Na(g) + O(g)$	15.56	−40286	[19,20]
$K_2O(liq) = 2K(g) + O(g)$	15.33	−36735	[20,21]
$ThO_2(liq) = Th(g) + 2O(g)$	20.43	−112807	[20–23]
$UO_2(liq) = U(g) + 2O(g)$	19.18	−100627	[20,22,24]
$PuO_2(liq) = Pu(g) + 2O(g)$	18.67	−91886	[20,22,25]

TABLE 2

Thermodynamic data for formation of gases included in the vaporization calculations ($\log_{10} K = A + B/T$)

Reaction	A	B	Source
$\frac{1}{2}O_2(g) = O(g)$	3.47	−13282	[20]
$Si(liq) = Si(g)$	6.00	−20919	[19]
$Si(liq) + \frac{1}{2}O_2(g) = SiO(g)$	2.51	8207	[19]
$Si(liq) + O_2(g) = SiO_2(g)$	−1.44	18326	[19]
$Mg(g) = Mg(g)$	0	0	[19] [a]
$Mg(g) + \frac{1}{2}O_2(g) = MgO(g)$	−1.19	3794	[20]
$Fe(liq) = Fe(g)$	6.35	−19704	[20]
$Fe(liq) + \frac{1}{2}O_2(g) = FeO(g)$	3.39	−9951	[19]
$Ca(g) = Ca(g)$	0	0	[19] [b]
$Ca(g) + \frac{1}{2}O_2(g) = CaO(g)$	−1.61	6128	[20]
$Al(liq) = Al(g)$	5.70	−15862	[20]
$Al(liq) + \frac{1}{2}O_2(g) = AlO(g)$	3.04	−2143	[20]
$Al(liq) + O_2(g) = AlO_2(g)$	−0.09	5523	[20]
$2Al(liq) + \frac{1}{2}O_2(g) = Al_2O(g)$	2.04	10232	[20]
$2Al(liq) + O_2(g) = Al_2O_2(g)$	−1.53	23021	[20]
$Ti(liq) = Ti(g)$	6.46	−23025	[19]
$Ti(liq) + \frac{1}{2}O_2(g) = TiO(g)$	4.31	−2101	[20]
$Ti(liq) + O_2(g) = TiO_2(g)$	−0.41	17926	[20]
$Na(g) = Na(g)$	0	0	[19] [c]
$Na(g) + \frac{1}{2}O_2(g) = NaO(g)$	−1.43	1287	[19]
$2Na(g) = Na_2(g)$	−4.31	4281	[19]
$2Na(g) + \frac{1}{2}O_2(g) = Na_2O(g)$	−7.00	11898	[21]
$K(g) = K(g)$	0	0	[19] [d]
$K(g) + \frac{1}{2}O_2(g) = KO(g)$	−1.28	959	[19]
$2K(g) = K_2(g)$	−3.94	2852	[19]
$2K(g) + \frac{1}{2}O_2(g) = K_2O(g)$	−7.29	13340	[21]
$Th(liq) = Th(g)$	5.96	−29600	[22]
$Th(liq) + \frac{1}{2}O_2(g) = ThO(g)$	2.75	3497	[23]
$Th(liq) + O_2(g) = ThO_2(g)$	−1.58	28875	[23]
$U(liq) = U(g)$	5.75	−25470	[22]
$U(liq) + \frac{1}{2}O_2(g) = UO(g)$	3.02	1705	[23]
$U(liq) + O_2(g) = UO_2(g)$	−1.19	26554	[23]
$U(liq) + \frac{3}{2}O_2(g) = UO_3(g)$	−4.24	43710	[23]
$Pu(liq) = Pu(g)$	4.79	−17316	[22]
$Pu(liq) + \frac{1}{2}O_2(g) = PuO(g)$	2.40	6875	[26]
$Pu(liq) + O_2(g) = PuO_2(g)$	−1.76	25984	[26]
$O_2(g) = O_2(g)$	0	0	[19] [e]

[a] $Mg(g)$ is the reference state at $T \geqslant 1378$ K [19].
[b] $Ca(g)$ is the reference state at $T \geqslant 1767.4$ K [19].
[c] $Na(g)$ is the reference state at $T \geqslant 1177$ K [19].
[d] $K(g)$ is the reference state at $T \geqslant 1044$ K [19].
[e] $O_2(g)$ is the reference state at all temperatures [19].

considered. Hydrogen-bearing gases (e.g., hydrides and hydroxides) were not included because the nebular gas is not in contact with the surface of the protoplanet [12], as discussed below, and an anhydrous magma is assumed.

The chemistry of the 11 metal oxides in the silicate magma was treated using two different models. The first model assumed an ideal solution of the 11 metal oxides in the magma. In this case the relationship between the thermodynamic activities (a_i) and concentrations (x_i = mole fraction) of the oxides in the magma is simply:

$$a_{\text{oxide}} = x_{\text{oxide}}. \qquad (2)$$

The second model assumed nonideal solution of the 11 metal oxides in the magma and thus the relationship between activity and concentration is:

$$a_{\text{oxide}} = f_{\text{oxide}} x_{\text{oxide}}, \qquad (3)$$

where f_i is the Raoultian activity coefficient (relative to the pure liquid oxides) for species i and is a function of temperature and concentration. No experimental data are available for the required activity coefficients at 3000 K or for such complex compositions. Furthermore, as discussed by Hastie and coworkers [14,16], available models developed for binary or ternary systems are unsuitable for multicomponent melts such as the silicate magma we are modelling. We therefore used an empirical model, the ideal mixing of complex components (IMCC) model, developed by Hastie and his colleagues, to calculate the chemistry of a nonideal silicate magma. This approach yields the

required activity coefficients as a function of temperature and concentration.

Briefly, the IMCC model considers a set of equilibria which reduce the concentrations of the
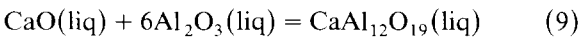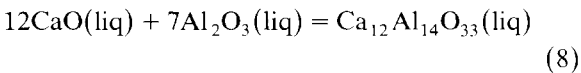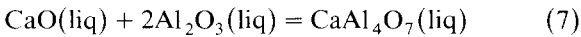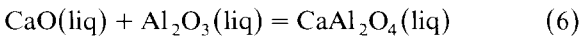
unbound (or free) metal oxides in the magma by formation of complex oxide and silicate pseudo-components (which we shall henceforth call "pseudospecies"). These pseudospecies are assumed to mix ideally in the melt. The equilibrium distribution of the metal oxides and pseudospecies is calculated by a standard method such as Gibbs free energy minimization. The activities of the metal oxides are then given by:

$$a_{\text{oxide}} = x^*_{\text{oxide}}, \tag{4}$$

where x_i^* is the mole fraction of unbound oxide i in the melt. This is equivalent to the relation:

$$f_i = x_i^*/x_i \tag{5}$$

for the activity coefficient of oxide i. For example, the concentrations of CaO and Al_2O_3 in the magma may be reduced by reactions such as:

$$CaO(liq) + Al_2O_3(liq) = CaAl_2O_4(liq) \tag{6}$$

$$CaO(liq) + 2Al_2O_3(liq) = CaAl_4O_7(liq) \tag{7}$$

$$12CaO(liq) + 7Al_2O_3(liq) = Ca_{12}Al_{14}O_{33}(liq) \tag{8}$$

$$CaO(liq) + 6Al_2O_3(liq) = CaAl_{12}O_{19}(liq) \tag{9}$$

as well as by reactions in other binary systems and in ternary systems (e.g., $CaO-Al_2O_3-SiO_2$). In the present work a total of 36 pseudospecies of the 8 oxides $SiO_2-MgO-FeO-CaO-Al_2O_3-TiO_2-Na_2O-K_2O$ was considered. The 3 metal oxides $UO_2-ThO_2-PuO_2$ were considered to mix ideally in the melt.

The relevant reactions and thermodynamic data for the pseudospecies are listed in Table 3. The selection of pseudospecies and the construction of the thermodynamic data base was influenced by several factors. Many components from the Hastie et al. [14,16] data base were included, but independent evaluations were made for the thermodynamic data. Where possible data from standard compilations such as the JANAF Tables and extrapolations of experimental data on silicate melts were used. In several cases it was necessary to estimate thermodynamic parameters involved in the calculation of the coefficients in Table 3. The details of the estimations and references to the specific literature sources are given by Fegley [27] and by Fegley and Kim [28] in reports available from M.I.T., which are summarized in Appendix 1.

The reader is referred to the papers by Hastie and coworkers [14–17] for a more comprehensive discussion of the IMCC model. However, we note that their work shows good agreement between the IMCC model predictions and available experimental vapor pressure and activity data for melts in the $Na_2O-K_2O-CaO-MgO-Al_2O_3-SiO_2$ system and subsystems. Furthermore, as we discuss later, the present work is in good agreement with compositional trends observed in vaporization experiments on chondritic material [29].

2.2. Method of calculation

Cameron [12], in his analysis of the vaporization of the mantle of protomercury under the assumed environmental conditions of the solar nebula, found that the removal of the vapors of silicate decomposition products by a nebula wind was a rather slow process, so that there was plenty of time for an atmosphere to form in equilibrium with the underlying magma. The base pressure of the atmosphere is thus the equilibrium pressure of the gas components which is a function of the assumed temperature. It turned out to be very difficult to mix nebular gases down to the base of the silicate atmosphere, and thus it is reasonable to neglect hydrogen-bearing compounds in these considerations of the equilibrium of the silicate decomposition products with the magma. There is a continual loss of atmosphere from its upper levels through the interaction with the nebular wind, so the composition of both the magma and the atmosphere change continually in time.

The effect of vaporization on the composition of the silicate magma was computed by us in a step-wise fashion. The step size was constrained by the requirement that the most rapidly depleted metal oxide (with $x_{\text{oxide}} > 10^{-16}$) was depleted by no more than 6% per step. In each step the magma was equilibrated with its vapor and the equilibrium compositions of both were calculated. The distribution of MgO and FeO between olivine and pyroxene was computed by assuming that SiO_2 formed as much pyroxene as it could, and if any SiO_2 was left over it was used up converting pyroxene to olivine. The relative proportions of metal and silicate, and the mean uncompressed density of the silicate and of the planet as a whole were calculated using the approximation that each component oxide had its natural uncompressed

TABLE 3

Thermodynamic data relating the activities of pseudospecies ($\log_{10} K = A + B/T$). See Appendix 1 for details

	Pseudoreaction	A	B
R1	$2MgO(liq) + SiO_2(liq) = Mg_2SiO_4(liq)$	-0.94	7434
R2	$MgO(liq) + SiO_2(liq) = MgSiO_3(liq)$	0.42	2329
R3	$MgO(liq) + Al_2O_3(liq) = MgAl_2O_4(liq)$	1.18	464
R4	$MgO(liq) + TiO_2(liq) = MgTiO_3(liq)$	-0.13	3246
R5	$MgO(liq) + 2TiO_2(liq) = MgTi_2O_5(liq)$	0.51	2845
R6	$2MgO(liq) + TiO_2(liq) = Mg_2TiO_4(liq)$	0.67	3812
R7	$3Al_2O_3(liq) + 2SiO_2(liq) = Al_6Si_2O_{13}(liq)$	-2.94	9375
R8	$CaO(liq) + Al_2O_3(liq) = CaAl_2O_4(liq)$	-1.89	10060
R9	$CaO(liq) + 2Al_2O_3(liq) = CaAl_4O_7(liq)$	-0.59	9713
R10	$12CaO(liq) + 7Al_2O_3(liq) = Ca_{12}Al_{14}O_{33}(liq)$	-6.30	72239
R11	$CaO(liq) + SiO_2(liq) = CaSiO_3(liq)$	0.54	5568
R12	$CaO(liq) + Al_2O_3(liq) + 2SiO_2(liq) = CaAl_2Si_2O_8(liq)$	2.63	5326
R13	$CaO(liq) + MgO(liq) + 2SiO_2(liq) = CaMgSi_2O_6(liq)$	1.46	8485
R14	$2CaO(liq) + MgO(liq) + 2SiO_2(liq) = Ca_2MgSi_2O_7(liq)$	0.63	15327
R15	$2CaO(liq) + Al_2O_3(liq) + SiO_2(liq) = Ca_2Al_2SiO_7(liq)$	2.01	10710
R16	$CaO(liq) + TiO_2(liq) = CaTiO_3(liq)$	-0.08	7055
R17	$2CaO(liq) + SiO_2(liq) = Ca_2SiO_4(liq)$	0.63	8416
R18	$CaO(liq) + TiO_2(liq) + SiO_2(liq) = CaTiSiO_5(liq)$	-0.18	10071
R19	$FeO(liq) + TiO_2(liq) = FeTiO_3(liq)$	-0.51	3569
R20	$2FeO(liq) + SiO_2(liq) = Fe_2SiO_4(liq)$	-0.63	3103
R21	$FeO(liq) + Al_2O_3(liq) = FeAl_2O_4(liq)$	-1.76	5692
R22	$CaO(liq) + 6Al_2O_3(liq) = CaAl_{12}O_{19}(liq)$	-3.79	22612
R23	$2MgO(liq) + 2Al_2O_3(liq) + 5SiO_2(liq) = Mg_2Al_4Si_5O_{18}(liq)$	7.48	0
R24	$Na_2O(liq) + SiO_2(liq) = Na_2SiO_3(liq)$	-1.33	13870
R25	$Na_2O(liq) + 2SiO_2(liq) = Na_2Si_2O_5(liq)$	-1.39	15350
R26	$\frac{1}{2}Na_2O(liq) + \frac{1}{2}Al_2O_3(liq) + SiO_2(liq) = NaAlSiO_4(liq)$	0.65	6997
R27	$\frac{1}{2}Na_2O(liq) + \frac{1}{2}Al_2O_3(liq) + 3SiO_2(liq) = NaAlSi_3O_8(liq)$	1.29	8788
R28	$\frac{1}{2}Na_2O(liq) + \frac{1}{2}Al_2O_3(liq) = NaAlO_2(liq)$	0.55	3058
R29	$Na_2O(liq) + TiO_2(liq) = Na_2TiO_3(liq)$	-1.38	15445
R30	$\frac{1}{2}Na_2O(liq) + \frac{1}{2}Al_2O_3(liq) + 2SiO_2(liq) = NaAlSi_2O_6(liq)$	-1.02	9607
R31	$K_2O(liq) + SiO_2(liq) = K_2SiO_3(liq)$	0.15	14600
R32	$K_2O(liq) + 2SiO_2(liq) = K_2Si_2O_5(liq)$	-0.73	18466
R33	$\frac{1}{2}K_2O(liq) + \frac{1}{2}Al_2O_3(liq) + SiO_2(liq) = KAlSiO_4(liq)$	0.97	8675
R34	$\frac{1}{2}K_2O(liq) + \frac{1}{2}Al_2O_3(liq) + 3SiO_2(liq) = KAlSi_3O_8(liq)$	1.11	11229
R35	$\frac{1}{2}K_2O(liq) + \frac{1}{2}Al_2O_3(liq) + KAlO_2(liq)$	0.72	4679
R36	$\frac{1}{2}K_2O(liq) + \frac{1}{2}Al_2O_3(liq) + 2SiO_2(liq) = KAlSi_2O_6(liq)$	1.53	10125

density. The vapor was then removed and the next step started. Because the Fe metal was assumed to form a core, it was not in contact with the vapor and was assumed to be undepleted. In a real planet there might be some mixing of such iron across the core-mantle interface, but such effects lie beyond the goals of this investigation. A related question is whether FeO can be reduced in the mantle and sink down to join the core. We have found that the oxygen fugacity is always high enough to prevent this.

Results of the vaporization calculations will now be discussed first for an ideal solution model and then for a nonideal solution model of the magma.

2.3. Vaporization of ideal silicate magma

Results of the vaporization calculations for the ideal solution case at 3000 K are shown in Figs. 1-4. Figs. 1 and 2 show the composition of the vapor atmosphere and the underlying mantle as a function of the remaining mantle mass fraction. The first elements lost during vaporization are the alkalis, Na and K, with K being more volatile. The
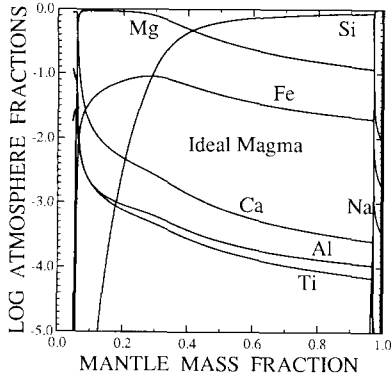
Fig. 1. The composition of the vapor atmosphere as a function of the mantle mass fraction that remains as the vaporization proceeds, for an ideal magma. The elements shown are balanced by oxygen in the atmosphere. The unlabelled line shown descending steeply right next to the right-hand edge of the frame is potassium.

Fig. 3. The density of the mantle as a function of the remaining mantle mass fraction as vaporization proceeds. The dashed line is for an ideal magma; the solid line is for a nonideal magma, both at 3000 K.

next element lost is Si, followed by Fe and Mg. At the highest degree of vaporization ($\sim$ 4.6% residual mantle mass fraction), $\sim$ 95% of the Al, $\sim$ 40% of the Ca, and $\sim$ 15% of the Ti remain in the mantle.

The calculated mantle density for this case, shown as the dashed line in Fig. 3, has a complicated structure. The density increases to a maximum at 3.71 g/cm^3 when approximately 28% of the original silicate remains. The mantle density then decreases with increasing vaporization until about 10% of the silicate remains and the density is about 3.65 g/cm^3. The density then starts in-

creasing again with further vaporization and is virtually indistinguishable from the density profile for the nonideal magma case. In contrast, the calculated mean uncompressed density of the planet, shown as the dashed line in Fig. 4, monotonically increases with the degree of vaporization. The uncompressed mean density of 5.3 g/cm^3 for Mercury is reached after about 72% of the mantle has been vaporized. The calculated composition of the silicate phase at this point is given in Table 4. The (possible) later accretion of ordinary silicate (MgO-, SiO$_2$-rich) planetesimals could change this composition by adding more SiO$_2$, FeO, and alkalis. However, the observed mean density of the planet could then only be obtained provided that more than 72% of the mantle had originally been

Fig. 2. The composition of the mantle as a function of its remaining mass fraction as vaporization proceeds, for an ideal magma. The elements shown are balanced by oxygen in the mantle. K is not shown because it coincides with the right frame starting close to the bottom.

Fig. 4. The density of the Mercury protoplanet as a function of the remaining mantle mass fraction as vaporization proceeds. The dashed line corresponds to an ideal magma; the solid line is for a nonideal magma, both at 3000 K.

TABLE 4

Predicted mantle and crust compositions from different vaporization models (mean uncompressed density $= 5.3$ g/cm^3)

Oxide	Mass % oxide in different models			
	1	2	3	4
SiO$_2$	1.2	32.1	25.9	19.9
CaO	9.9	14.6	13.7	11.7
MgO	67.7	34.5	42.3	50.0
Al$_2$O$_3$	12.4	18.1	17.0	14.4
FeO	8.3	0.0	0.4	3.4
TiO$_2$	0.5	0.7	0.8	0.6
K (ppb)	0.0	0.0	0.0	0.0
U (ppb) [a]	0.0	0.0	0.0	0.3
Th (ppb) [a]	278	401	377	322

[a] Primordial abundances 4.55×10^9 years ago.

Models: 1 = ideal magma, 3000 K; 2 = nonideal magma, 2500 K; 3 = nonideal magma, 3000 K; 4 = nonideal magma, 3500 K.

vaporized and lost, leaving the remaining fraction of the original mantle even more refractory.

Finally, the heat-producing radionuclides behave in two quite different fashions during vaporization. Loss of K occurs early during the vaporization process. The K abundance is down to 10^{-6} of the initial abundance after only about 0.5% of the silicate has been vaporized. U is also lost during vaporization and is depleted much more than Pu (approximately as volatile) or Th (less volatile). This is due to the formation of volatile U-oxide gases. In contrast, Pu and Th are essentially undepleted by vaporization by the time that the mean uncompressed planetary density of 5.3 g/cm^3 is reached.

2.4. Vaporization of nonideal silicate magma

Models with nonideal silicate magma were run at 2500, 3000, and 3500 K, which are representative of the expected temperatures at the position of formation of Mercury during the dissipation of the solar nebula to form the Sun [12,13]. The results of the exemplary 3000 K model are displayed in Figs. 3–9; those of the other two models are given in Table 4. Figs. 5 and 6 give the compositions of the vapor atmosphere and the underlying mantle, and should be compared with Figs. 1 and 2. Figs. 7–9 show the abundances of the pseudospecies in the mantle for, respectively, compounds of silicon, alkalis, and magnesium (ex-
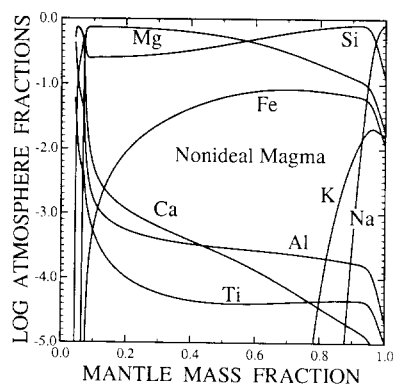
Fig. 5. The composition of the vapor atmosphere as a function of the mantle mass fraction that remains as the vaporization proceeds, for a nonideal magma. The elements shown are balanced by oxygen in the atmosphere.

cept for pseudospecies of very low abundance). The solid lines in Figs. 3 and 4 show the densities of the mantle and planet for the nonideal case.

These runs display several interesting features. The alkalis are still the most volatile elements but Fe is the next element lost, followed by Si and Mg. However, Mg loss from the magma accelerates after about 80% of the silicate has been vaporized. At the highest degree of vaporization considered (96% of original silicate lost), more Si remains in the magma than Mg. Loss of Ca and Ti is also occurring at this point. More Ti (53%) but less Ca (33%) remains in the magma relative to the ideal magma case.

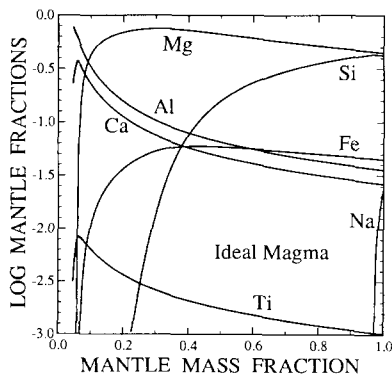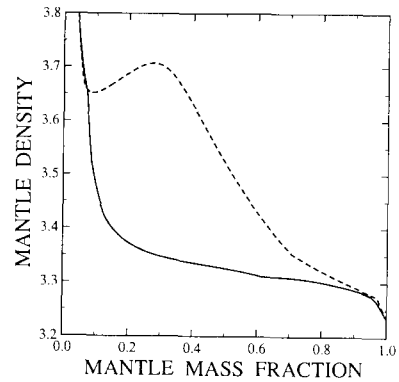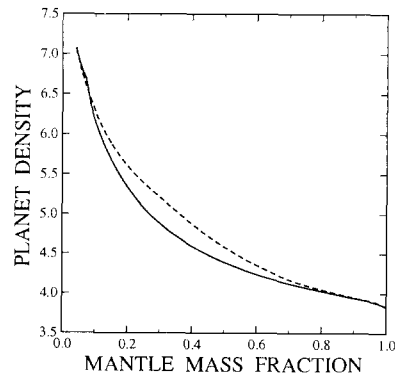Figs. 7–9 illustrate some of the complex chem-

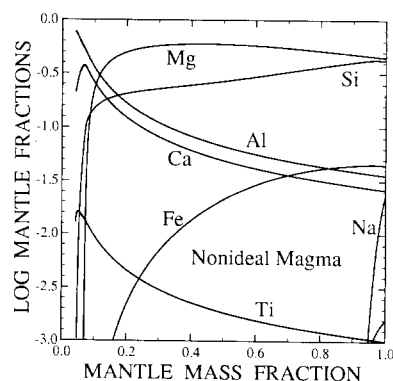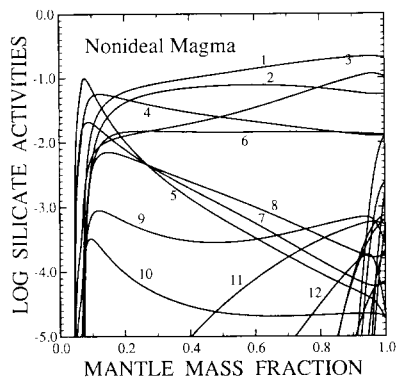Fig. 6. The composition of the mantle as a function of its remaining mass fraction as vaporization proceeds, for a non-ideal magma. The elements shown are balanced by oxygen in the mantle. The unlabelled line in the lower right corner is potassium.
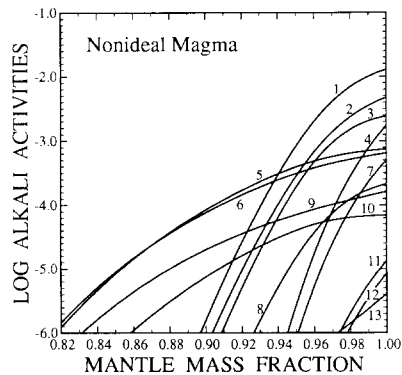
Identification of Pseudospecies:

1. MgSiO$_3$	2. Mg$_2$SiO$_4$	3. SiO$_2$
4. CaSiO$_3$	5. Ca$_2$Al$_2$SiO$_7$	6. CaMgSi$_2$O$_6$
7. Ca$_2$SiO$_4$	8. Ca$_2$MgSi$_2$O$_7$	9. CaAl$_2$Si$_2$O$_8$
10. CaTiSiO$_5$	11. Fe$_2$SiO$_4$	12. Mg$_2$Al$_4$Si$_5$O$_{18}$

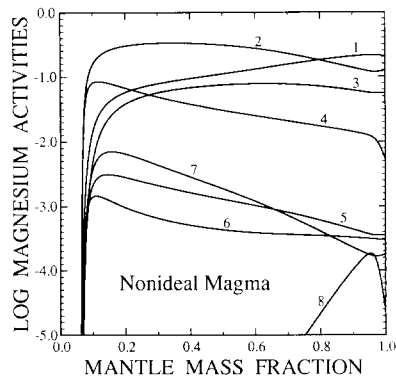The cluster of lines descending steeply at the right-hand edge are sodium and potassium pseudospecies.

Fig. 7. The abundances of pseudospecies containing silicates in a nonideal magma at 3000 K, as a function of the mantle mass fraction which remains as vaporization proceeds. The pseudospecies are identified below the figure, except for the alkali pseudospecies. Some of the silicate pseudospecies listed in Table 3 are too low in abundance to appear on this graph.

Identification of Pseudospecies:

1. MgSiO$_3$	2. MgO	3. Mg$_2$SiO$_4$
4. MgAl$_2$O$_4$	5. Mg$_2$TiO$_4$	6. MgTiO$_3$
7. Ca$_2$MgSi$_2$O$_7$	8. Mg$_2$Al$_4$Si$_5$O$_{18}$	

Fig. 9. The abundances of pseudospecies containing magnesium oxides in a nonideal magma at 3000 K, as a function of the mantle mass fraction which remains as vaporization proceeds. The pseudospecies are identified below the figure. Some of the silicate pseudospecies listed in Table 3 are too low in abundance to appear on this graph.

istry in the nonideal silicate magma. The alkalis Na and K are the most nonideal metals considered. The activity coefficients for Na$_2$O and K$_2$O

Identification of Pseudospecies:

1. NaAlSiO$_4$	2. NaAlO$_2$	3. NaAlSi$_3$O$_8$
4. Na$_2$SiO$_3$	5. KAlSi$_2$O$_6$	6. KAlSiO$_4$
7. Na$_2$Si$_2$O$_5$	8. NaAlSi$_2$O$_6$	9. KAlO$_2$
10. KAlSi$_3$O$_8$	11. Na$_2$TiO$_3$	12. Na$_2$O
13. K$_2$SiO$_3$		

Fig. 8. The abundances of pseudospecies containing alkali oxides in a nonideal magma at 3000 K, as a function of the mantle mass fraction which remains as vaporization proceeds. The pseudospecies are identified below the figure. Some of the alkali pseudospecies listed in Table 3 are too low in abundance to appear on this graph.

in the magma are about 10^{-4} and 10^{-7}, respectively (relative to pure liquid oxides), at 3000 K and only 3% vaporization. These activity coefficients decrease with decreasing Na and K in the melt (increasing degrees of vaporization). The major Na- and K-bearing pseudospecies in the magma are aluminosilicates and aluminates. Similar results are obtained at 2500 and 3500 K. Hastie et al. [14–17] present experimental data and model calculations displaying qualitatively similar behavior for Na and K in a variety of oxide and silicate melts, although at much lower temperatures.

The other metal oxides in the melt also exhibit negative deviations from ideality, although not as pronounced as those shown by the alkalis. The precise nature of these deviations is a function of temperature and composition (i.e., of the degree of vaporization). However, several general trends are observed. The FeO activity coefficients are in the range of 0.90–0.99 for all 3 runs. Activity coefficients for TiO$_2$ are in the range of 0.1–0.3 for SiO$_2$-, MgO-rich melts and are in the range of 0.04–0.1 for MgO-CaO-Al$_2$O$_3$ melts and CaO-Al$_2$O$_3$ melts.

The activity coefficients for SiO$_2$, MgO, CaO, and Al$_2$O$_3$ are more sensitive to temperature and composition variations. Higher temperatures at a

given composition lead to smaller deviations from ideality. As the magma composition changes during vaporization (at 3000 K) and becomes more CaO-, and Al_2O_3-rich, the CaO activity coefficients increase from about 0.01–0.02 to about 0.1–0.2, the Al_2O_3 activity coefficients decrease slightly from about 0.2–0.25 to about 0.09–0.15, and the ratio of the MgO to SiO_2 activity coefficients goes from less than unity to greater than unity. The trend in the MgO and SiO_2 activity coefficients agrees with the trend deduced from spinel solubilities in $CaO-Al_2O_3$ melts and experimental data on the $CaO-SiO_2-Al_2O_3$ system [30,31]. The variations in the CaO and Al_2O_3 activity coefficients are also qualitatively similar to the trends found in $CaO-Al_2O_3-SiO_2$ melts at 1873 K [32]. However, although the Al_2O_3 activity coefficients in these melts decrease with decreasing SiO_2 content (at constant Al_2O_3 and increasing CaO content) they are greater than unity. We are unaware of data for FeO and TiO_2 in the relevant melts so no comparisons can be made in these cases. Also, we caution that the available literature data are at temperatures 600–1600 K lower than our model runs. More comprehensive experimental work on silicate melt solution thermodynamics is required to better constrain the IMCC model at these extremely high temperatures.

However, since we are primarily interested in compositional variations as a function of the degree of vaporization, it is instructive to compare our calculations with the experimental results of Hashimoto [29]. In both cases Fe is the first major element (excluding the alkalis which Hashimoto did not consider) lost during vaporization. The initially more rapid Si loss (relative to Mg) and the reversal of their volatilities are also seen in the experimental work. Finally, the steadily increasing Al_2O_3 concentration and the turnover in the CaO concentration (at high degrees of vaporization) are also confirmed by Hashimoto's work. No Ti was included in the experiments but its concentration in the vaporization residue and its subsequent loss at the highest degree of vaporization ($\geq 96\%$ silicate lost) are expected, given the refractory nature of TiO_2 and Ti-bearing oxides such as $CaTiO_3$, which are nonetheless slightly more volatile than the Al_2O_3 phases (e.g., see the calculated condensation sequence in [30]). Thus, the major fea-

tures of the nonideal magma vaporization calculations are confirmed by vaporization experiments. We will now discuss the predictions of our vaporization calculations for the composition of Mercury.

3. Discussion

3.1. Model compositions for Mercury

Table 4 gives model compositions for the silicate phase (crust and mantle) of Mercury for the four vaporization models discussed in sections 2.3 and 2.4. In each case the calculated mean uncompressed planetary density is 5.3 g/cm^3, which matches the value deduced for Mercury. Approximately 79% of the silicate must be lost by vaporization in the nonideal case to bring the density of the planet up to this value.

All four compositions in the Table are depleted in the alkalis, FeO, and SiO_2, and are enriched in CaO, MgO, Al_2O_3, and TiO_2 relative to chondritic material. There is a large difference, which brackets the end-member compositions expected from vaporization of a silicate magma, between the results of the ideal and nonideal models. Further discussion centers on the latter models because of the good agreement of these runs with the available data on silicate vaporization and activity coefficients which was reviewed earlier.

3.2. Specific predictions of vaporization models for Mercury's composition and structure

We matched the uncompressed planetary mean density with a metal to silicate mass ratio of approximately 64 : 36, with the silicate phase considerably reduced in SiO_2 relative to some of the metal oxides. Inclusion of Ni in the metal phase will decrease slightly the calculated metal abundance because Ni is denser than Fe (8.90 vs. 7.86 g/cm^3, respectively). However, this is a second-order effect; an alloy with the solar Ni abundance and Fe decreased by forming FeO = 0.1 MgO (as in our models) is only 0.8% denser than pure Fe.

Second, the silicate phase is predicted to be depleted in the alkalis, FeO, and SiO_2 and enriched in CaO, MgO, Al_2O_3, and TiO_2 relative to chondritic material. The vaporization models also predict that the silicate is depleted in SiO_2 and enriched in other oxides (CaO, MgO, Al_2O_3, TiO_2, and FeO) relative to silicate compositions calculated for equilibrium condensation models of
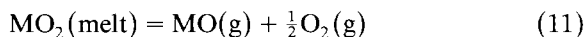
Mercury [3]. These differences will influence several aspects of Mercury's composition and structure including (a) the mineralogy of the silicate phase, (b) the nature of a crust (if a distinct, differentiated crust exists), (c) the chemical composition and physical properties, such as viscosity, of volcanic magmas, and (d) trace element partitioning between putative magmas and their source regions.

Finally, unique trace element abundance patterns are predicted by the vaporization models. The oxygen fugacities (f_{O_2}) produced during vaporization range from $\log_{10} f_{O_2} = -0.8$ (3500 K) to -3.6 (2500 K) for the compositions given in Table 4. These f_{O_2} values are significantly higher than canonical solar nebula oxygen fugacities [33] ranging from $\log_{10} f_{O_2} = -14.4$ (1900 K) to -19.3 (1400 K) assumed to prevail during condensation of planetary-forming material [4]. The high f_{O_2} values during vaporization can cause depletions of refractory trace elements which form volatile oxide gases. The elements will then be depleted relative to other elements of similar volatility which are either not oxidized at all, or which are less easily oxidized.

This effect is responsible for the depletion of U relative to Pu and Th because of the different vaporization reactions for these elements. U vaporizes predominantly by the reaction:

$$UO_2(\text{melt}) + \tfrac{1}{2}O_2(g) = UO_3(g) \qquad (10)$$

while Pu and Th vaporize by the reactions:

$$MO_2(\text{melt}) = MO(g) + \tfrac{1}{2}O_2(g) \qquad (11)$$

$$MO_2(\text{melt}) = MO_2(g) \qquad (12)$$

where M is either Pu or Th. Increases in f_{O_2} will drive reaction (10) to the right (increasing the volatility of U) but will drive reaction (11) to the left (decreasing the volatilities of Pu and Th) and will not affect reaction (12) at all. Similar effects will also control the vaporization behavior of other sets of elements with similar volatilities but with different tendencies to be oxidized.

In particular, several rare earth elements (REE) are reliably reported to form dioxide gases, which have been observed above the evaporating REE oxides by mass spectrometry [34–37]. These REE are Ce, Pr, Nd, and Tb. Under the high oxygen fugacities due to the magma vaporization, these oxides can then vaporize according to the general

reaction:

$$M_2O_3(\text{melt}) + \tfrac{1}{2}O_2(g) = 2MO_2(g), \qquad (13)$$
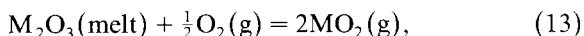
where M = Ce, Pr, Nd, Tb. However, the REE which do not form dioxide gases can only vaporize according to the general reactions:

$$M_2O_3(\text{melt}) = 2MO(g) + \tfrac{1}{2}O_2(g) \qquad (14)$$

$$M_2O_3(\text{melt}) = 2M(g) + \tfrac{3}{2}O_2(g) \qquad (15)$$
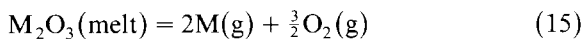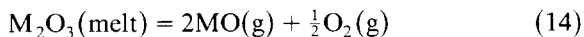
where M is any REE (including Ce, Pr, Nd, Tb). Again the effect of high oxygen fugacities will be to drive reaction (13) to the right while driving reactions (14) and (15) to the left. In this case depletions are predicted for the REE which form dioxide gases relative to REE of similar volatilities which do not form the dioxide gases.

The precise nature of these predicted depletions is a function of several factors including temperature, f_{O_2} (partially dependent on melt composition), the REE oxide activity coefficients, and the relative stabilities of the monatomic, monoxide, and dioxide gases. The quantitative consideration of all these factors is outside the scope of this work. However, Ce depletions, which have been explained by formation under f_{O_2} values 10^3 to 10^4 times greater than the canonical solar nebula f_{O_2} values [38,39], have been observed in several Ca,Al-rich inclusions in chondrites [40–42]. Thus Ce depletions are expected in the vaporization models which yield much higher oxygen fugacities. Depletions in the other REE observed to form dioxide gases (Pr, Nd, Tb) are also a distinct possibility.

The observation of such highly fractionated REE patterns and of U depletions relative to Th in the silicates on Mercury would be a unique indicator of extensive vaporization. In the absence of any vaporization, the REE, U, and Th, which are completely condensed by the Fe condensation temperature [33,43], would be expected to be present in relative chondritic proportions. This is in fact the case for the ratio of any two refractory elements (e.g., Sm/Nd, Lu/Hf) that is carefully determined in the Earth, the Moon, or the Eucrite Parent Body [44]. However, these relative chondritic ratios will be severely perturbed by the postulated vaporization. These effects would be separate from and much larger than (see [40–42]) REE partitioning during ordinary geochemical processes.

3.3. Shortcomings of the equilibrium condensation model

Several authors have noted that the qualitatively appealing but unrealistically simple equilibrium condensation model [4] is unable to account for the high uncompressed mean density of Mercury without recourse to special mechanisms (e.g., aerodynamic sorting) or to an unrealistically narrow accretion zone [3,7,45,46]. Basically, the problem is that the condensation temperatures of Fe metal and of magnesium silicates ($MgSiO_3$ and Mg_2SiO_4) are so close together that the two phases cannot be separated during accretion. Hence the recourse to a special mechanism for removal of silicate grains or for concentration of metal grains.

If condensation occurred under conditions more oxidizing than solar (as suggested by Mo and W depletions in many Ca-, Al-rich inclusions [33]), then this problem is exacerbated because silicate condensation temperatures increase with increases in oxygen fugacity while that of Fe metal remains constant [47].

On the other hand, if condensation occurred under conditions more reducing than solar (as apparently happened for the enstatite chondrites [48]), then the silicate condensation temperatures decrease with decreases in oxygen fugacity while that of Fe metal remains constant [48]. However, there are several problems with such a scenario. Large separations in the Fe metal and Mg_2SiO_4 condensation temperatures are not obtained until f_{O_2} values exist corresponding to carbon/oxygen ratios of about unity. No astrophysically reasonable mechanisms for changing the nebular C/O ratio from the solar value of 0.6 to the required value of unity have been proposed. Perhaps more disturbing is the condensation of another suite of minerals including elemental carbon (graphite), SiC, CaS, MgS, AlN, and TiN instead of ordinary silicates at C/O ratios above one. The large amounts of graphite ($\rho = 2.25$ g/cm^3) make the production of a high density, iron-rich planet dependent upon special mechanisms for separating 2.5 times as much graphite (by mass) from the Fe metal. However, this problem can be avoided by assuming that condensation occurs at C/O ratios just below one where graphite will not form [48]. But in this case the other unusual minerals still form in preference to ordinary silicates. There

is no evidence from remote sensing for this exotic mineralogy on the surface of Mercury, which resembles the lunar surface ([45] and references therein). Finally, the mineral cohenite (Fe_3C) replaces Fe at a C/O ratio of unity. Cohenite is 2% less dense than Fe metal, but cannot be ruled out solely on this basis. It should be noted that equilibrium condensation under conditions sufficiently reducing to decrease significantly the silicate condensation temperatures (but not to produce graphite) predicts a volatile-rich Mercury containing about 12% of the solar carbon abundance, 4% of the solar nitrogen abundance, and 100% of the solar sulfur abundance.

3.4. Possible spacecraft experiments

Several different experiments may prove useful for testing the predictions of the vaporization model and for distinguishing between it and competing hypotheses. The most useful experiments appear to be those which will yield information on the major element chemistry, mineralogy, and trace element chemistry of the silicate interior. Chemical analyses of the surface may reflect the later accretion of ordinary silicates after the end of the dissipation phase of the solar nebula, and thus be unrepresentative of planetary bulk silicate compositions. With this caveat in mind, the desirable experiments include: (a) geochemical analyses for both major elements (Si, Mg, Ca, Al, Ti, Na, K, O, C, N , S, Fe, Ni) and trace elements (REE, Th, U), particularly around unfilled basins where samples of the deep interior may be exposed; (b) establishment of a seismic net with at least three stations; (c) measurement of the polar moment of inertia (C/MR^2) to better than 5% to help constrain interior structure models; and (d) measurement of the global heat flow. We emphasize that analyses of the REE and actinides are potentially very important for distinguishing between the vaporization model (which is expected to produce large depletions in U, Ce, Pr, Nd, and Tb) and competing hypotheses which are expected to yield essentially chondritic ratios of the REE and other refractory trace elements.

4. Summary

We have modelled the vaporization of a totally molten silicate magma for protomercury by using

ideal and nonideal descriptions of the magma chemistry. An empirical model, the ideal mixing of complex components (IMCC) model, developed by Hastie and coworkers [14–17] was used to describe the nonideal magma.

The results of our calculations show the changes in composition of the silicate magma and of the vapor in equilibrium with it as a function of the degree of vaporization at temperatures of 2500–3500 K. Comparison of the results of the nonideal magma calculations with experimental work on vaporization of chondritic material shows generally good agreement. In particular, both our calculations and the experimental work display the same major trends during vaporization.

We find that vaporization of about 70–80% of the original amount of silicate from a chondritic planet is required to produce an iron-rich body with a mean uncompressed density equal to that deduced for Mercury (5.3 g/cm^3). At this point the silicate is depleted in the alkalis, FeO, and SiO$_2$, and enriched in CaO, MgO, Al$_2$O$_3$, and TiO$_2$ relative to chondritic material. The compositions (nonideal magma runs at 2500, 3000, 3500 K) are also depleted in SiO$_2$ and enriched in other oxides (CaO, MgO, Al$_2$O$_3$, TiO$_2$, and FeO) relative to silicate compositions calculated for equilibrium condensation models of Mercury. Another prediction of our vaporization models is the production of trace element abundance patterns which are depleted in easily oxidized elements relative to other trace elements of similar volatilities. In particular, the depletion of U, Ce and of other easily oxidized REE is expected. These abundance patterns are unique signatures due to vaporization and are not produced in other competing models.

Acknowledgements

Appendix 1 — Thermodynamic data for reactions in Table 3

The thermodynamic data sources and estimation methods used to derive the A and B coefficients given in Table 3 are briefly described below. The pseudoreactions are referred to by the numbering scheme used in Table 3. the Gibbs free energies for formation of solid and liquid MgO, SiO$_2$, FeO (stoichiometric), CaO, Al$_2$O$_3$, Na$_2$O, and TiO$_2$ are all from JANAF [19,20]. The Gibbs free energy for formation of K$_2$O(s) is from JANAF [19] and the Gibbs free energy for formation of K$_2$O (liquid) is from Glushko et al. [21]. The Gibbs free energies for formation of the pseudospecies from the constituent oxides are either calculated directly (e.g., from JANAF data) or from a thermodynamic cycle. In the latter case, the Gibbs free energy change for formation of the solid oxide (from the elements or from the constituent oxides) is combined with the Gibbs free energy difference between the solid and liquid phases (e.g. between solid and liquid CaSiO$_3$) and (as appropriate to close the cycle) with the Gibbs free energy of formation of the constituent oxide liquids from the elements or with the Gibbs energy difference between the solid and liquid phases of each constituent oxide. The details of the method used for each reaction are described below.

Details of the specific uncertainties for each set of A and B coefficients can be found by consulting the references listed below; however, some general statements regarding these uncertainties can be made. Typical uncertainties in entropies of melting may be ± 8.4 J/(mol K) [16]; these lead to typical uncertainties in enthalpies of melting of ± 16.7 kJ/mol for a melting point of 2000 K. Typical errors in heat capacities may be $\pm(4-8)$ J/(mol K); Kubaschewski and Alcock [50] and Kelley [51] discuss heat capacity estimates and give comparisons to experimental values for a large number of inorganic compounds. The JANAF Tables should also be consulted for estimates of typical uncertainties in high temperature thermodynamic data.

Finally, note that the abbreviation g atom is g mol atoms, i.e., 1 mole of Al$_2$O$_3$ contains 5 gram mole atoms.

R1–R6: All data from JANAF [19,20].

R7: JANAF data for liquid Al$_2$O$_3$ and SiO$_2$ and for solid mullite. The Gibbs free energy difference between solid and liquid Al$_6$Si$_2$O$_{13}$ (as a function of temperature) is derived from the heat capacity of mullite, the mullite melting point given by JANAF (2023 K), the heat of fusion (113 kJ/mol) calculated by Risbud and Pask [49] and the estimated heat capacity of liquid Al$_6$Si$_2$O$_{13}$ (34.5 J/(g atom K)) based on the weighted average of liquid Al$_2$O$_3$ and SiO$_2$ heat capacities per g atom. This heat capacity estimate is made using standard techniques employed by groups such as JANAF [19,20], Kubaschewski and Alcock [50], and Kelly [51]. For reference, the experimentally measured heat contents for liquid Al$_2$O$_3$ and SiO$_2$ yield liquid heat capacities of 38.5 J/(g atom K) and 28.6 J/(g atom K), respectively, as summarized by JANAF.

R8: The Gibbs free energy for formation of liquid CaAl$_2$O$_4$ from the constituent solid oxides is taken from Rein and Chipman [32] and combined with JANAF data for CaO(s), liquid CaO, α-Al$_2$O$_3$, and liquid Al$_2$O$_3$.

R9: The Gibbs free energy for formation of $CaAl_4O_7(s)$ from the constituent solid oxides is taken from Allibert et al. [52]. More recent work by Blander and Pelton [53] confirms this equation. The Gibbs free energy difference between solid and liquid $CaAl_4O_7$ (as a function of temperature) was derived from the $CaAl_4O_7$ melting point (2035 K) given by Nurse et al. [54], an estimated entropy of melting (11.3 J/(g atom K)) and an estimated $CaAl_4O_7$ liquid heat capacity (31.4 J/(g atom K)). These estimated values are consistent with the experimental values for solid and liquid Al_2O_3 and with recommended estimates for the entropy of melting and the heat capacity of liquids [19,20,50, 51].

R10: See discussion for R8. The Gibbs free energy for formation of $Ca_{12}Al_4O_{33}$ from the constituent solid oxides was taken from Rein and Chipman [32].

R11: The drop calorimetry measurements (900–1850 K) of Richet and Bottinga [55] combined with the heat capacity [51,56] for pseudowollastonite give the Gibbs free energy difference between solid and liquid $CaSiO_3$ as a function of temperature. Data from Robie et al. [56] for formation of pseudowollastonite from the constituent elements and JANAF [19,20] data for formation of liquid CaO and SiO_2 from the elements then yield the coefficients for R11. The calculated Gibbs free energy change for R11 is in good agreement with values calculated from the work of Rein and Chipman [32] at 1700–1900 K and from the experimental heat content measurements of Stout and Piwinskii [57] on $CaSiO_3$ at 1700–2600 K.

R12: Same method as used for R11. The heat of melting of $CaAl_2Si_2O_8$ and the heat capacity of the liquid are taken from Richet and Bottinga [55]. The heat capacity of anorthite and its Gibbs free energy of formation from the constituent elements are taken from Kelley [51] and Hemingway et al. [58].

R13: Same method as used for R11. The heat of melting of $CaMgSi_2O_6$, the heat capacity of the liquid, and the heat capacity of diopside are taken from the drop calorimetric study of Stebbins et al. [59]. The Gibbs free energy of formation of diopside from the elements is from Robie et al. [56]. Similar coefficients are obtained for R13 using the drop calorimetry of Richet and Bottinga [55] and Stout and Piwinskii [57] or using the work of Rein and Chipman [32].

R14: Same method as used for R11. The heat of melting of $Ca_2MgSi_2O_7$ and the heat capacity of the liquid are taken from the drop calorimetry work of Proks et al. [60]. The heat capacity of akermanite and its Gibbs free energy of formation from the constituent elements are taken from Pankratz and Kelley [61] and Robie et al. [56].

R15: The heat capacity of gehlenite and its Gibbs free energy of formation from the elements are taken from Pankratz and Kelley [61] and Hemingway et al. [58]. The entropy of melting (6.0 J/(g atom K)) and the heat capacity of liquid $Ca_2Al_2SiO_7$ (31.8 J/(g atom K)) are taken equal to the respective values for akermanite [60].

R16: The heat capacity of perovskite and its Gibbs free energy of formation from the elements are taken from Kelley [51] and Robie et al. [56]. The entropy of melting (9.6 J/g atom K)) and the heat capacity of liquid $CaTiO_3$ (32.7 J/(g atom K)) are estimates based on the mean of experimentally determined values for Na and Li titanates [51].

R17: The heat capacity of larnite and its Gibbs free energy of formation from the elements are taken from Kelley [51] and Hemingway et al. [58]. The entropy of melting (7.3 J/(g atom K)) and the heat capacity of liquid Ca_2SiO_4 (33.5 J/(g atom K)) are estimates based on the mean of the experimental values for $CaSiO_3$ and $CaMgSi_2O_6$.

R18: The heat capacity of solid and liquid $CaTiSiO_5$ and the heat of melting are from Kelley [51]. The Gibbs free energy for formation of solid $CaTiSiO_5$ from the elements is from Robie et al. [56].

R19: The heat capacity of solid and liquid $FeTiO_3$ and the heat of melting are from Kelley [51]. The Gibbs free energy for formation of solid $FeTiO_3$ from the elements is from Robie et al. [56].

R20: The heat capacity of solid and liquid Fe_2SiO_4 and the heat of melting are from Kelley [51]. The Gibbs free energy for formation of solid Fe_2SiO_4 from the elements is from Robie et al. [56].

R21: The Gibbs free energy for formation of solid $FeAl_2O_4$ from the elements was taken from the experimental measurements of Chan et al. [62]. The heat capacity for solid $FeAl_2O_4$ is from Kelley [51]. The entropy of melting (8.8 J/g atom K)) and the heat capacity of liquid $FeAl_2O_4$ (34.3 J/(g atom K)) are estimates consistent with standard estimation techniques [19,20,50,51] and with JANAF [20] data on liquid $MgAl_2O_4$.

R22: See discussion for R9. The Gibbs free energy for formation of solid $CaAl_{12}O_{19}$ from the constituent solid oxides is taken from Allibert et al. [52]. More recent work by Blander and Pelton [53] confirms this equation. The Gibbs free energy difference between solid and liquid $CaAl_{12}O_{19}$ (as a function of temperature) was calculated from the $CaAl_{12}O_{19}$ melting point given by Nurse et al. [54], an estimated heat capacity for solid and liquid $CaAl_{12}O_{19}$ (28.0 J/(g atom K) and 38.5 J/(g atom K), respectively, based on solid and liquid Al_2O_3), and an

estimated entropy of melting (9.5 J/(g atom K)) based on Al_2O_3.

R23: The heat capacity of solid $Mg_2Al_4Si_5O_{18}$ and its Gibbs free energy for formation from the elements are taken from Pankratz and Kelley [61] and Robie et al. [56]. The heat of melting (11.9 kJ/(g atom)) at the estimated metastable congruent melting point (1740 K) and the heat capacity of liquid Mg_2-$Al_4Si_5O_{18}$ are taken from the drop calorimetry work of Richet and Bottinga [55].

R24–R25: All data from JANAF [19].

R26: The heat capacity of nepheline and its Gibbs free energy of formation from the elements are taken from Kelley [51] and Robie et al. [56]. The heat of melting (7.0 kJ/g atom) and the heat capacity of liquid $NaAlSiO_4$ (31.6 J/(g atom K)) are from the drop calorimetry work of Stebbins et al. [59]. Stebbins et al. estimate the metastable $NaAlSiO_4$ (nepheline) melting point as 1750 K.

R27: The Gibbs free energy for formation of $NaAlSi_3O_8$ (analbite) from the elements is taken from Robie et al. [56]. The heat capacities of solid and liquid $NaAlSi_3O_8$ and the heat of melting are taken from Stebbins et al. [59].

R28: The Gibbs free energy for formation of $NaAlO_2$ solid from the elements was calculated by the third law method (described by JANAF [19]). Gibbs energy functions for $NaAlO_2(s)$ are from the heat capacity [51] and the entropy at 298 K [63]. Gibbs energy functions for the constituent elements are from JANAF [19,20]. The heat of formation of $NaAlO_2(s)$ at 298 K is from the National Bureau of Standards Compilation [63]. The entropy of melting (7.3 J/(g atom K)) and the heat capacity of liquid $NaAlO_2$ (34.6 J/(g atom K)) are estimated as the values for $NaBO_2$ [64].

R29: See discussion for R28. The Gibbs free energy for formation of $Na_2TiO_3(s)$ from the elements was calculated by the third law method using the $Na_2TiO_3(s)$ heat capacity [51], entropy at 298 K and heat of formation at 298 K [63]. Gibbs energy functions for the constituent elements are from JANAF [19,20]. The entropy of melting is from Kelley [51] and the heat capacity of liquid Na_2TiO_3 (35.4 J/(g atom K)) is the mean heat capacity calculated from the data of Richet and Bottinga [65].

R30: The Gibbs free energy for formation of jadeite from the elements is from Robie et al. [56]. The heat capacity for jadeite is from Kelley [51]. Extrapolation of the results of Bell and Roseboom [66] to 1 bar pressure yields a metastable melting point of 1325 K. The entropy of melting and heat

capacity of liquid $NaAlSi_2O_6$ estimated to be the same as $NaAlSi_3O_8$ are 3.5 J/(g atom K) and 28.4 J/(g atom K), respectively.

R31: The Gibbs free energies for formation of liquid SiO_2 and K_2SiO_3 from the elements are taken from JANAF [19,20], the values for liquid K_2O are taken from Glushko et al. [21].

R32: The Gibbs free energy for formation of K_2Si_2-$O_5(s)$ from the constituent solid oxides, the heat of melting, and the heat capacity for liquid $K_2Si_2O_5$ are from Beyer et al. [67].

R33: The Gibbs free energy for formation of $KAlSiO_4(s)$ from the elements and the heat capacity are from Robie et al. [56]. The melting point (2033 K) is taken from Schairer and Bowen [68]. The entropy of melting (4.0 J/(g atom K)) and the heat capacity of liquid $KAlSiO_4$ (31.6 J/(g atom K)) are estimated by analogy with the experimental values for $NaAlSiO_4$.

R34: The Gibbs free energy for formation of $KAlSi_3O_8$ (high sanidine) from the elements is from Robie et al. [56]. The heat capacity of solid and liquid $KAlSi_3O_8$, the heat of melting, and the estimated congruent melting point (1473 K) are from Stebbins et al. [59].

R35: The Gibbs free energy for formation of liquid $KAlO_2$ is taken from Glushko et al. [21].

R36: The Gibbs free energy for formation of leucite from the elements is from Robie et al. [56]. The heat capacity for leucite is from Pankratz [69]. The melting point (1959 K) is from Schairer and Bowen [68]. The entropy of melting (3.0 J/(g atom K)) was estimated from the experimental data for $KAlSi_3O_8$ [59]. The heat capacity of liquid $KAlSi_2O_6$ (29.6 J/(g atom K)) was estimated as the mean of the experimental values for $NaAlSi_3O_8$, $KAlSi_3O_8$, and $NaAlSiO_4$.

References

1 H.C. Urey, The origin and development of the Earth and other terrestrial planets, Geochim. Cosmochim. Acta 1, 209–277, 1951.

2 H.C. Urey, The Planets, Yale University Press, New Haven, Conn., 1952.

3 Basaltic Volcanism Study Project, Basaltic Volcanism on the Terrestrial Planets, Pergamon, New York, N.Y., 1981.

4 J.S. Lewis, Metal/silicate fractionation in the solar system, Earth Planet. Sci. Lett. 15, 286–290, 1972.

5 P.G. Harris and D.C. Tozer, Fractionation of iron in the solar system, Nature 215, 1449–1451, 1967.

6 E. Orowan, Density of the Moon and nucleation of planets, Nature 222, 867, 1969.

7 S.J. Weidenschilling, Iron/silicate fractionation and the origin of Mercury, Icarus 35, 99–111, 1978.

8 J.V. Smith, Mineralogy of the planets: a voyage in space and time, Mineral. Mag. 43, 1–89, 1979.

9 G. Wetherill, unpublished, 1985.

10 K.E. Bullen, Cores of terrestrial planets, Nature 170, 363–364, 1952.

11 A.E. Ringwood, Chemical evolution of the terrestrial planets, Geochim. Cosmochim. Acta 30, 41–104, 1966.

12 A.G.W. Cameron, The partial volatilization of Mercury, Icarus 64, 285–294, 1985.

13 A.G.W. Cameron, Formation and evolution of the primitive solar nebula, in: Protostars and Planets II, D. C. Black and M.S. Matthews, eds., pp. 1073–1099, University of Arizona Press, Tucson, Ariz., 1985.

14 J.W. Hastie and D.W. Bonnell, A. predictive phase equilibrium model for multicomponent oxide mixtures, II. Oxides of Na-K-Ca-Mg-Al-Si, High Temp. Sci. 19, 275–306, 1985.

15 J.W. Hastie, D.W. Bonnell, E.R. Plante and W.S. Horton, Thermodynamic activity and vapor pressure models for silicate systems including coal slags, in: Thermochemistry and Its Applications to Chemical and Biochemical Systems, M.A.V. Ribeiro da Silva, ed., pp. 235–251, D. Reidel, Dordrecht, 1984.

16 J.W. Hastie, W.S. Horton, E.R. Plante and D.W. Bonnell, Thermodynamic models of alkali-metal vapor transport in silicate systems, High Temp. High Press. 14, 669–679, 1982.

17 J.W. Hastie, E.R. Plante and D.W. Bonnell, Alkali vapor transport in coal conversion and combustion systems, in: Metal Bonding and Interactions in High Temperature Systems, J.L. Gole and W.C. Stwalley, eds., pp. 543–600, American Chemical Society, Washington, D.C., 1982.

18 E. Anders and M. Ebihara, Solar-system abundances of the elements, Geochim. Cosmochim. Acta 46, 2363–2380, 1982.

19 D.R. Stull and H. Prophet, eds., JANAF Thermochemical Tables, 2nd ed., NSRDS-NBS 37, Washington, D.C., 1971.

20 M.W. Chase, J.L. Curnutt, A.T. Hu, H. Prophet, A.N. Syverud, L.C. Walker, J.R. Downey, Jr., R.A. McDonald and E.A. Valenzuela, eds., JANAF Supplements, Dow Chemical Co., Midland, Mich., 1971–1985.

21 V.P. Glushko, L.V. Gurvich, G.A. Bergman, I.V. Veitz, V.A. Medvedev, G.A. Khachkuruzov and V. S. Yungman, eds., Thermodynamic Properties of Individual Substances, 4 volumes, High Temperature Institute, Moscow, 1978–1982.

22 F.L. Oetting, M.H. Rand and R.J. Ackermann, The Chemical Thermodynamics of Actinide Elements and Compounds, Part 1. The Actinide Elements, I.A.E.A., Vienna, 1976.

23 R.J. Ackermann and M.S. Chandrasekharaiah, Systematic thermodynamic properties of actinide metal-oxygen systems at high temperatures in: Thermodynamics of Nuclear Materials 1974, Vol. 2, pp. 3–26, I.A.E.A., Vienna, 1975.

24 D.W. Green and L. Leibowitz, Vapor pressures and vapor compositions in equilibrium with hypostoichiometric uranium dioxide at high temperatures, Argonne National Laboratory Rep. ANL-CEN-RSD-81-1, 1981.

25 D.W. Green, J.K. Fink, and L. Leibowitz, Vapor pressures and vapor compositions in equilibrium with hypostoichio-

metric plutonium dioxide at high temperatures, Argonne National Laboratory Rep. ANL-CEN-RSD-82-1, 1982.

26 D.W. Green, Tables of thermodynamic functions for gaseous thorium, uranium, and plutonium oxides, Argonne National Laboratory Rep. ANL-CEN-RSD-80-1, 1980.

27 B. Fegley, Jr., A thermodynamic data base for a chemical equilibrium code to model vaporization equilibria of multicomponent oxide melts, Planetary Chemistry Laboratory Rep. No. 9, M.I.T. Industrial Liaison Program, 1986.

28 B. Fegley, Jr. and N. Kim, Thermodynamic data for sodium and potassium compounds for a chemical equilibrium code to model vaporization equilibria of multicomponent oxide melts, Planetary Chemistry Laboratory Rep. No. 10, M.I.T. Industrial Liaison Program, 1986.

29 A. Hashimoto, Evaporation metamorphism in the early solar nebula—evaporation experiments on the melt FeO-MgO-SiO$_2$-CaO-Al$_2$O$_3$ and chemical fractionations of primitive materials, Geochem. J. 17, 111–145, 1983.

30 M. Blander and L.H. Fuchs, Calcium-aluminum-rich inclusions in the Allende meteorite: evidence for a liquid origin, Geochim. Cosmochim. Acta 39, 1605–1619, 1975.

31 D.A.R. Kay and J. Taylor, Activities of silica in the lime + alumina + silica system, Trans. Faraday Soc. 56, 1372–1386, 1960.

32 R.H. Rein and J. Chipman, Activities in the liquid solution SiO$_2$-CaO-MgO-Al$_2$O$_3$ at 1600 C, Trans. A.I.M.E. 233, 415–425, 1965.

33 B. Fegley, Jr. and H. Palme, Evidence for oxidizing conditions in the solar nebula from Mo and W depletions in refractory inclusions in carbonaceous chondrites, Earth Planet. Sci. Lett. 72, 311–326, 1985.

34 M.B. Panish, Vaporization of several rare earth oxides, J. Chem. Phys. 34, 1079–1080, 1961.

35 S.A. Shchukarev and G.A. Semenov, Mass spectrometric study of the vapor composition above rare earth oxides, Dokl. Akad. Naúk S.S.S.R. 141, 652–654, 1961.

36 H.G. Staley and J.A. Norman, Thermodynamics of gaseous monoxide-dioxide equilibria for cerium, praesodymium and neodymium, Int. J. Mass. Spectrom. Ion Phys. 2, 35–43, 1969.

37 D. White, P.N. Walsh, L.L. Ames and H.W. Goldstein, Thermodynamics of vaporization of the rare-earth oxides at elevated temperatures; dissociation energies of the gaseous monoxides, in: Thermodynamics of Nuclear Materials, pp. 417–443, I.A.E.A. Symp. Proc., 1962.

38 W.V. Boynton, Rare-earth elements as indicators of supernova condensation, Lunar Planet. Sci. IX, 120–122, 1978.

39 B. Fegley, Jr., A comparison of REE and refractory metal oxidation state indicators for the solar nebula, Lunar Planet. Sci. XVII, 220–221, 1986.

40 R. Conard, A study of the chemical composition of Ca,Al-rich inclusions from the Allende meteorite, 129 pp., M.S. Thesis, Oregon State University, 1976.

41 A.M. Davis, T. Tanaka, L. Grossman, T. Lee and G.J. Wasserburg, Chemical composition of HAL, and isotopically-unusual Allende inclusion, Geochim. Cosmochim. Acta 46, 1627–1651, 1982.

42 R.W. Hinton, A.M. Davis and D.E. Scatena-Wachel, Ion microprobe determination of REE and other trace elements in meteoritic hibonite, Lunar Planet. Sci. XVI, 352–353, 1985.

43 A.S. Kornacki and B. Fegley, Jr., The abundance and relative volatility of refractory trace elements in Allende Ca,Al-rich inclusions: implications for chemical and physical processes in the solar nebula, Earth Planet. Sci. Lett. 79, 217–234, 1986.

44 H. Palme and K.G. Nickel, Ca/Al ratio and the composition of the Earth's upper mantle, Geochim. Cosmochim. Acta 49, 2123–2132, 1985.

45 J.S. Lewis and R.G. Prinn, Planets and their Atmospheres. Origin and Evolution, Academic Press, New York, N.Y., 1984.

46 S.S. Barshay, Combined condensation-accretion model of the terrestrial planets, 62 pp., Ph.D. Thesis, M.I.T., 1981.

47 H.A. Bartholomay and J.W. Larimer, Dust-gas fractionation in the early solar system, Meteoritics 17, 180–181, 1982.

48 J.W. Larimer and M. Bartholomay, The role of carbon and oxygen in cosmic gases: some applications to the chemistry and mineralogy of enstatite chondrites, Geochim. Cosmochim. Acta 43, 1455–1466, 1979.

49 S.H. Risbud and J.A. Pask, Calculated thermodynamic data and metastable immiscibility in the system SiO_2-Al_2O_3, J. Am. Ceram. Soc. 60, 418–424, 1977.

50 O. Kubaschewski and C.B. Alcock, Metallurgical Thermochemistry, 5th ed., Pergamon Press, Oxford, 1979.

51 K.K. Kelley, Contributions to the data on theoretical metallurgy, XIII. High-temperature heat content, heat capacity and entropy data for the elements and inorganic compounds, U.S. Bur. Mines Bull. 584, 1960.

52 M. Allibert, C. Chatillon, K.T. Jacob and R. Lourtau, Mass-spectrometric and electrochemical studies of thermodynamic properties of liquid and solid phases in the system CaO-Al_2O_3, J. Am. Ceram. Soc. 64, 307–314, 1981.

53 M. Blander and A.D. Pelton, Computer-assisted analysis of the thermodynamic properties of slags in coal combustion systems, Argonne National Laboratory, Rep. ANL/FE-83-19, 1983.

54 R.W. Nurse, J.H. Welch and A.J. Majumdar, The CaO-Al_2O_3 system in a moisture-free atmosphere, Trans. Brit. Ceram. Soc. 64, 409–418, 1965.

55 P. Richet and Y. Bottinga, Anorthite, andesine, wollastonite, diopside, cordierite and pyrope: thermodynamics of melting, glass transitions, and properties of the amorphous phases, Earth Planet. Sci. Lett. 67, 415–432, 1984.

56 R.A. Robie, B.S. Hemingway and J.R. Fisher, Thermodynamic properties of minerals and related substances at 298.15 K and 1 bar (10^5 pascals) pressure and at higher temperatures, U.S. Geol. Surv. Bull. 1452, 1979.

57 N.D. Stout and A.J. Piwinskii, Enthalpy of silicate melts from 1520 to 2600 K under ambient pressure, High Temp. Sci. 15, 275–292, 1982.

58 B.S. Hemingway, J.L. Haas, Jr. and G.R. Robinson, Jr., Thermodynamic properties of selected minerals in the system Al_2O_3-CaO-SiO_2-H_2O at 298.15 K and 1 bar (10^5 pascals) pressure and at higher temperatures, U.S. Geol. Surv. Bull. 1544, 1982.

59 J.E. Stebbins, I.S.E. Carmichael and D.E. Weill, The high temperature liquid and glass heat contents and the heat of fusion of diopside, albite, sanidine and nepheline, Am. Mineral. 68, 717–730, 1983.

60 I. Proks, M. Eliasova and L. Kosa, The heat of fusion of akermanite, Silikaty 21, 3–11, 1977.

61 L.B. Pankratz and K.K. Kelley, High-temperature heat contents and entropies of akermanite, cordierite, gehlenite, and merwinite, U.S. Bur. Mines RI 6555, 1964.

62 J.C. Chan, C.B. Alcock and K.T. Jacob, Electrochemical measurement of the oxygen potential of the system iron-alumina-hercynite in the temperature range 750 to 1600 C, Can. Metall. Q. 12, 439–443, 1973.

63 D.D. Wagman, W.H. Evans, V.B. Parker, R.H. Schumm and R.L. Nuttall, Selected values of chemical thermodynamic properties: compounds of uranium, protactinium, thorium, actinium, and the alkali metals, National Bureau of Standards Tech. Note 270-8, 1981.

64 W. Slough and G.P. Jones, A compilation of thermodynamic data for borate systems, National Physical Laboratory Rep. Chem. 31 1974.

65 P. Richet and Y. Bottinga, Heat capacity of aluminum-free silicate liquids, Geochim. Cosmochim. Acta 49, 471–486, 1985.

66 P.M. Bell and E.H. Roseboom, Jr., Melting relationships of jadeite and albite to 45 kilobars with comments on melting diagrams of binary systems at high pressures, Min. Soc. Am. Spec. Pap. 2, 151–161, 1969.

67 R.P. Beyer, M.J. Ferrante, R.R. Brown and G.E. Daut, Thermodynamic properties of potassium metasilicate and disilicate, U.S. Bur. Mines RI 8410, 1979.

68 J.F. Schairer and N.L. Bowen The system K_2O-Al_2O_3-SiO_2, Am. J. Sci. 253, 681–746, 1985.

69 L.B. Pankratz, High-temperature heat contents and entropies of dehydrated analcite, kaliophilite, and leucite, U.S. Bur. Mines RI 7073, 1968.